Increasing tap density of carbon-coated Na3V2(PO4)2F3 via mechanical grinding: good or bad idea?

Gaël Minart, Laurence Croguennec, François Weill, Christine Labrugère-Sarroste, Jacob Olchowka

Increasing tap density of carbon-coated $Na_3V_2(PO_4)_2F_3$ via mechanical grinding: Good or bad idea?

Gaël Minart[1,2], Laurence Croguennec[1,2,3], François Weill[1,2], Christine Labrugère-Sarroste[4], Jacob Olchowka[1,2,3,*]

[1] CNRS, Univ. Bordeaux, Bordeaux INP, ICMCB UMR 5026, F-33600 Pessac, France.

[2] RS2E, Réseau Français sur le Stockage Electrochimique de l'Energie, FR CNRS 3459, F-80039 Amiens Cedex 1, France.

[3] ALISTORE-ERI European Research Institute, FR CNRS 3104, F-80039 Amiens Cedex 1, France.

[4] Univ. Bordeaux, CNRS, PLACAMAT, UAR 3626, F-33600 Pessac, France.

KEYWORDS: Na-ion Batteries, Positive electrode material, $Na_3V_2(PO_4)_2F_3$, Tap density, Mechanical grinding, self-discharge

Corresponding author: jacob.olchowka@icmcb.cnrs.fr

Abstract:

Polyanionic positive electrode materials like $Na_3V_2(PO_4)_2F_3$ are renowned for their exceptional rate performance and long-term stability during cycling. However, they present low tap densities that penalize the volumetric energy density when it comes to practical applications. In this study, we successfully increased the tap density of carbon-coated $Na_3V_2(PO_4)_2F_3$ by 40% through mechanical grinding of dense particles previously obtained via solid-state reaction, resulting in an impressively high tap density of 1.4 g/cm^3. Comprehensive structural and microstructural investigations revealed that this mechanical process reduces both particle and crystallite sizes without affecting the structure or the composition of the active material. Besides extensive electrochemical experiments, including evaluation of capacity retention upon long-term cycling and at high rates, electrochemical impedance spectroscopy as well as self-discharge tests, were conducted to assess the impact of the change in microstructure on the energy storage performance. Furthermore, thermal stability assessments of electrodes in contact with electrolyte and at different states of charge were also performed to complete the study and provide a complete overview of the influence of such mechanical grinding processes commonly employed in the field of energy storage.

Introduction

The limited abundance of lithium in the Earth's crust, coupled with the exponentially increasing demand for energy storage devices, has driven extensive research in the field of Na-ion batteries over the last decade.[1,2] In this regard, various families of positive electrode materials, namely sodium layered transition metal oxides, Prussian blue analogs (PBA) and polyanionic compounds have emerged as excellent candidates for large-scale development of Na-ion batteries.[3–5] Each family has its intrinsic advantages and drawbacks that need to be addressed to achieve optimized performance in terms of energy and power density as well as long-term cyclability.[6,7] For instance, layered oxides possess high theoretical capacity but are sensitive to moisture and exhibit complex phases transition during charge/discharge cycle that limits their performance. For this family, it makes difficult to find the good compromise between composition, structure and properties.[8] On the other hand, PBAs, despite being cheap and based on abundant elements, suffer from low electronic conductivity and possess structural defects, such as structural water molecules, that negatively impact the cycling stability and lead to safety concerns in case of thermal runaway.[9,10] Dealing with polyanionic compounds, although their capacity is limited due to electrochemically inactive polyanionic groups, their stable 3D structural framework usually undergo low volume changes upon repeated Na^+ insertion and extraction, resulting in excellent long-term stability and rate capability.[11,12]

Among the various phosphate, sulfate, pyrophosphate and other polyanionic compounds investigated as positive electrode materials, $Na_3V_2(PO_4)_2F_3$ (NVPF) stands out due to its high working potential and attractive reversible capacity (128 $mAh.g^{-1}$ for the reversible extraction of 2 Na^+ per formula unit at ~3.9 V vs Na^+/Na).[13–17] Additionally, the first 18650 prototypes built with carbon-coated NVPF (NVPF@C) at the positive electrode have demonstrated excellent rate performance and cycling stability, making this material ideal for high-power applications.[17] However, as for the PBA and the other polyanionic electrode materials, NVPF suffers from low tap density, which is one of the most important parameters when it comes to practical applications.[8,18,19] A low tap density ($g.cm^{-3}$) reduces the amount of material that can be introduced in a defined volume, such as a cylindrical 18650 cell, leading to poor volumetric energy density. Furthermore, it necessitates thick electrode for high mass loading, which penalizes the power density.

The common strategy for increasing tap density involves adjusting the particles size and morphology through modification of the synthesis conditions.[20,21] For example, researchers at Faradion company successfully achieved a 30% increase in tap density of layered transition metal oxides from Generation 1 to Generation 2, by developing dense spherical aggregates of approximately 20 µm in diameter.[19] For $Na_3V_2(PO_4)_2F_3$ or its derivatives $Na_3V_2(PO_4)_2F_{3-y}O_y$, the few data available in the literature report tap density between 0.8 and 1.2 g/cm^3, which is comparable to the value estimated for other polyanionic electrode materials such as $Na_3V_2(PO_4)_3$ or Na_2FePO_4F (see Table 1).[22–29] Direct synthesis of nanoparticles, and growing particles with a platelet morphology or in a porous template, result in an active material with a low tap density (0.8 to 1 g/cm^3). The highest tap density values (1.2 g/cm^3) are reported for microsphere particles obtained by an annealing at high temperature after a first low-temperature shaping chemical process such as spray drying.[26] However, such low-temperature shaping often leads to porous precursors in the case of carbon-coated $Na_3V_2(PO_4)_2F_3$ (NVPF@C) which finally limits the final tap density.

To tackle this issue, the innovative approach we used in this study consists in first obtaining dense and well crystallized micrometric particles of NVPF@C via a classical solid-state synthesis and then, shaping them by mechanical grinding to increase the tap density. This work clearly demonstrates the efficiency of such approach as the tap density was increased by 40% leading to extremely favorable value of 1.4 g/cm^3, which is, to the best of our knowledge, the highest value reported for such polyanionic electrode materials. Additionally, detailed structural and electrochemical investigations were carefully conducted to examine the impact of this post annealing particles shaping on the electrode material and on its energy storage performance.

Table 1. Comparison of the tap density and particles morphology for different polyanionic positive electrode materials.

Composition	Morphology	Tap density	Reference
$Na_3V_2(PO_4)_2F_3$	Microspheres	1.1 g/cm^3	[22]
$Na_3V_2(PO_4)_2F_3$	Irregular particles	0.85 g/cm^3	[22]
$Na_3V_2(PO_4)_2F_3$	Microspheres	0.92 g/cm^3	[22]
$Na_3V_2(PO_4)_2FO_2$	Sub-microspheres	0.86 g/cm^3	[23]
$Na_3V_2(PO_4)_2FO_2$	Micrometric platelets	0.8 g/cm^3	[24]
$Na_3V_2(PO_4)_2F_3$/C@RGO	Sub-micrometric particles (300 nm)	1.01 g/cm^3	[25]
$Na_3V_2(PO_4)_2F_3$@C/CNT	Microspheres	1.2 g/cm^3	[26]
$Na_3V_2(PO_4)_2FO_2$@P/N/C	Microspheres	1.22 g/cm^3	[30]
$Na_3V_2(PO_4)_2F_3$@C/CNT	Nanoparticles	1.04 g/cm^3	[27]
$Na_3V_2(PO_4)_2F_3$	Nanoparticles	1.15 g/cm^3	[27]
Na_2FePO_4F@C@MCNTs	Microspheres	1.2 g/cm^3	[28]
$Na_3V_2(PO_4)_3$@C@RGO	Macroporous 3D structure	0.8 g/cm^3	[29]
$Na_3V_2(PO_4)_2F_3$@C	Sub-micro and micrometric particles	1.4 g/ cm^3	This work

Experimental Section

Materials preparation:

Carbon-coated $Na_3V_2(PO_4)_2F_3$ (NVPF@C) was obtained via a one-step solid-state synthesis. First, stoichiometric amounts of carbon-coated VPO_4 (c-VPO_4) and NaF (Sigma Aldrich; ≥ 99%) were thoroughly grinded in a mortar. Then, the mixture was pelletized, placed in a gold crucible and heated at 600°C for 3 hours under Argon flow.

Further 5g of NVPF@C were mechanically grinded in a 45 mL agate jar (SPEX) with five 10 mm agate beads for 60 minutes and 90 minutes, giving rise to NVPF@C-60 and NVPF@C-90 respectively. Finally, these two materials were washed for 1 day in a large excess of distilled water under stirring, recovered by centrifugation and dried at 80°C for 16 hours. The effect of the washing step is discussed in the supporting information part.

X-ray diffraction: XRD patterns were measured on a Panalytical Empyrean diffractometer in Bragg-Bentano θ-θ geometry. The powder diffraction patterns were recorded with a spinning flat samples holder in the 2θ range of 10°-110° with a 0.0167° step size. A copper $K\alpha_{1,2}$ type source was used for X-rays emission and refinements were performed using the FullProf software.

Scanning electron microscopy: Polycrystalline samples were deposited on a carbon film and undergone a gold deposition on the surface. Then, SEM images were acquired with a Tescan Vega instrument at various magnifications.

Transmission electron microscopy (TEM) images were obtained with a JEOL 2100 microscope. NVPF@C was dispersed in ethanol and a drop was deposited on a copper grid with a carbon supported film to conduct the experiment.

Granulometry: The NVPF@C particles diameter size distribution was obtained by laser granulometry using a Malvern MASTERSIZER 2000. The powders were dispersed by ultrasounds in ethanol, the suspension flowing then in a closed loop.

Tap Density measurements: The powders tap densities (in g/cm^3) were measured with an AUTOTAP from Quantachrome Instruments. For each sample, 1.5 g to 2 g of powder were disposed in a 20 ± 0.1 mL graduated cylinder and tapped 10 000 times. A small quantity of particles could stay not densified after the hits sequence, they were carefully removed in order to not alter the volume measurement. The tap density corresponds to the mass of NVPF@C divided by the volume reached in the graduated cylinder after the 10 000 hits.

Raman spectroscopy data were obtained with a confocal LabRAM HR Evolution micro-spectrometer from Horiba, using a 633 nm laser source. The spectra were collected using a 10.6 mm (NA 0.5) focal length lens and with an acquisition time of 30 s and 30 accumulations.
For each sample Raman measurements were performed at different points of the samples as detailed in supporting information.

XPS spectra were recorded with a ThermoFisher Scientific K-ALPHA spectrometer with a monochromatized Al-Kα source (hν = 1486.6 eV) and a 400 µm X-Ray spot size. The powders were pressed onto indium foils. The full spectra (0-1150 eV) were obtained with a constant pass energy of 200 eV, while high-resolution spectra were recorded with a constant pass energy of 40 eV. Charge neutralisation was applied during the analysis, and depth profiles were fulfilled with an Ar^+ ion gun. High resolution spectra (i.e. C1s, O1s, V2p, P2p, Na1s, F1s) were quantified using the Avantage software provided by ThermoFisher Scientific by applying Scofield sensitivity factors. All spectra were shifted versus C1s main peak at 284.6 eV. Main attention was paid on C 1s, V 2p3/2 and F 1s spectra to get the chemical environment after fitting.

Differential scanning calorimetry Differential scanning calorimetry was performed using a DSC Pyris Diamond calorimeter. The samples consisted of scraped electrodes recovered at different states of charge. For each experiment, 8 to 12 mg were collected in a glovebox under Ar atmosphere and sealed in a high-pressure gold-plated stainless-steel crucible. This latter was heated in the 50-350°C temperature range with a 10°C.min^{-1} rate under argon flow (40 ml.min^{-1}).

Battery preparation. Electrodes were prepared using the tape casting method. 80 wt.% of active material (NVPF@C), 10 wt.% of carbon black and 10 wt.% of polyvinylidene fluorine were mixed in N-methyl-2-pyrrolidone (Sigma Aldrich; 99% anhydrous) for 20 minutes with a XENOX MHX/E equipped with a mixing nozzle. The slurry was casted on an aluminum foil with a 200 µm thickness and dried at 80°C overnight. The active mass loading of the electrodes was around 7 and 5 mg.cm^{-2} and the porosity around 35% and 27% for the pristine and grinded NVPF@C, respectively. After calendering at 5 tons, the average thickness of NVPF@C was 50±4 µm versus 30±3 µm for NVPF@C-90 (Table 2). The cells were assembled in an argon filled glovebox in CR2032-type coin cells with sodium metal used as negative electrode and 85 µL of electrolyte. This latter is composed of a mixture of ethylene carbonate and dimethyl carbonate in a 1:1 ratio by volume with 1 molar of $NaPF_6$ and 2% of fluoroethylene carbonate as an additive. The self-discharge was evaluated by subjecting the cells to three series of three charge and discharge cycles at C/20 rate (exchange of 1 electron in 20h) separated by 10 days of relaxation (open-circuit). Electrochemical impedance spectroscopy analyses (EIS) were conducted in the 10^6-10^{-2} Hz frequency window with two analyses per cell separated by three cycles at C/20.

Table 2. Summary of electrode's characteristics.

Sample	Electrode porosity	Active mass loading	Electrode thickness	Active mass Density
NVPF@C	35%	7 mg.cm²	50 µm	0.175 g/cm^3
NVPF@C-90	27%	5 mg.cm²	30 µm	0.208 g/cm^3

Results and discussion

NVPF@C obtained by solid-state reaction was mechanically ball-milled during 60 minutes and 90 minutes giving rise to samples called NVPF@C-60 and NVPF@C-90 respectively, as detailed in the experimental part.

The comparison of the X-ray diffraction patterns of the NVPF@C series (Figure 1a and Figures S1 - S3) demonstrates that the structure of the polyanionic phase remains intact after the ball-milling process. All the diffraction peaks measured for NVPF@C-60 and NVPF@C-90 can be indexed in the *Amam* space group with very similar lattice parameters for the two materials to those of the pristine NVPF@C (Table 3). On the other hand, although the samples remain well

crystallized, their coherent domains have decreased from > 1000 Å to 820 Å and 690 Å for NVPF@C-60 and NVPF@C-90 respectively. The integrity of the carbon-coating also seems to be preserved during the ball-milling process. As displayed in figure 1b, the Raman spectra of the three materials are very similar and no significant difference could be observed, especially neither in the shape nor in the intensity ratio between D-band and G-band. These two bands, corresponding to the so-called disordered sp^3 (D-band) and graphitic sp^2 (G-band), are the finger print of the carbon and are related to the nature and concentration of defects.[31] More details on Raman analyses, supported by images of the carbon coating by transmission electron microscopy, are given in Figures S4 - S6.

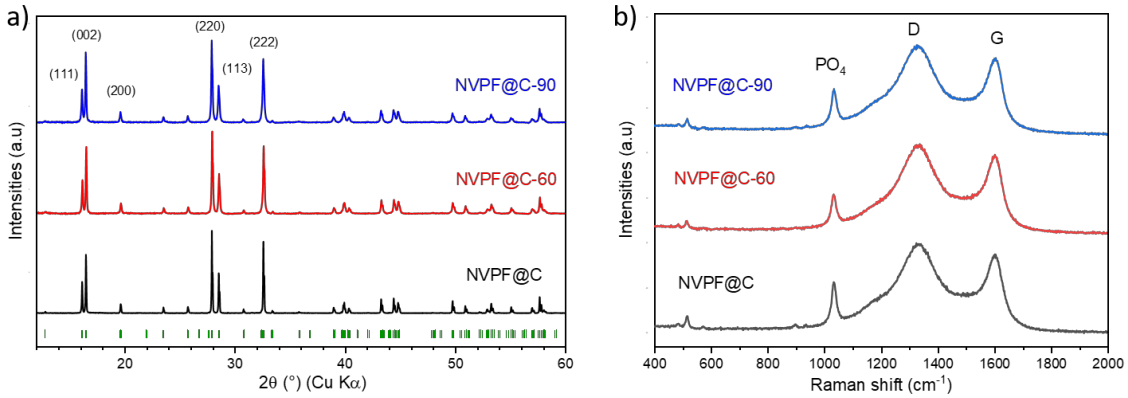

Figure 1. Comparison of a) X-ray diffraction patterns and b) Raman spectra between the samples before (NVPF@C) and after ball-milling (NVPF@C-60 and NVPF@C-90). The green ticks in figure 1a correspond to the theoretical positions of the reflections for $Na_3V_2(PO_4)_2F_3$ in Amam space group [32].

Concerning NVPF particles, as expected, their size tends to decrease after the mechanical grinding. As illustrated in Figure 2a-c and Figure S7, the shapeless micrometric particles characteristic of NVPF@C obtained by solid-state synthesis become much smaller after 60 and 90 minutes of ball milling and the big aggregates (> 10 µm) are much less numerous. Some aggregates can still be observed for NVPF@C-90 but they seem to be less numerous than for NVPF@C-60 when comparing several areas during the images' acquisitions. The progressive particle size reduction can be more clearly quantified by comparing the particle size distribution obtained by laser granulometry for the three samples. Figure 2d reveals that NVPF@C is characterized by a bimodal particle size distribution. The polycrystalline sample is composed of a majority of micrometric particles with a size distribution centered around 5 µm and a second population with a submicrometric particle size. The ratio between these two particles size populations reverses after the mechanical grinding and this inversion is more pronounced with the longer ball-milling process, in agreement with the previous SEM observations. Indeed, a significant change in the particle size distribution is observed after 60 minutes of mechanical grinding whereas additional 30 minutes process have a less pronounced impact. After 90 minutes of ball-milling, the particles with a size around 1 micrometer are predominant compared to those with a size around 10 µm. Such mixture of small and bigger particles has been reported to be beneficial for packing density and therefore, can lead to higher volumetric density in practical devices.[33]

On the other hand, the ball-milling has a rather minor impact on the specific surface area. Quite surprisingly in a first approach when considering the significant particle size reduction, the specific surface area only slightly increased from 14.9 m^2/g for NVPF@C to 15.4 m^2/g and 15.9 m^2/g for NVPF@C-60 and NVPF@C-90 respectively (Table 3). However, it should be noticed that the main contribution to this specific surface area comes from the carbon-coating. Typical specific surface area for $Na_3V_2(PO_4)_2F_3$ obtained by solid-state synthesis are reported around 2 m^2/g.[34] Thus, as previously suggested by Raman spectroscopy data, the minor changes in the specific surface area comfort the preservation of the carbon-coating integrity. This is also supported by TEM images (Figure S8) , revealing a continuous carbon coating on the particles surface after the mechanical grinding.

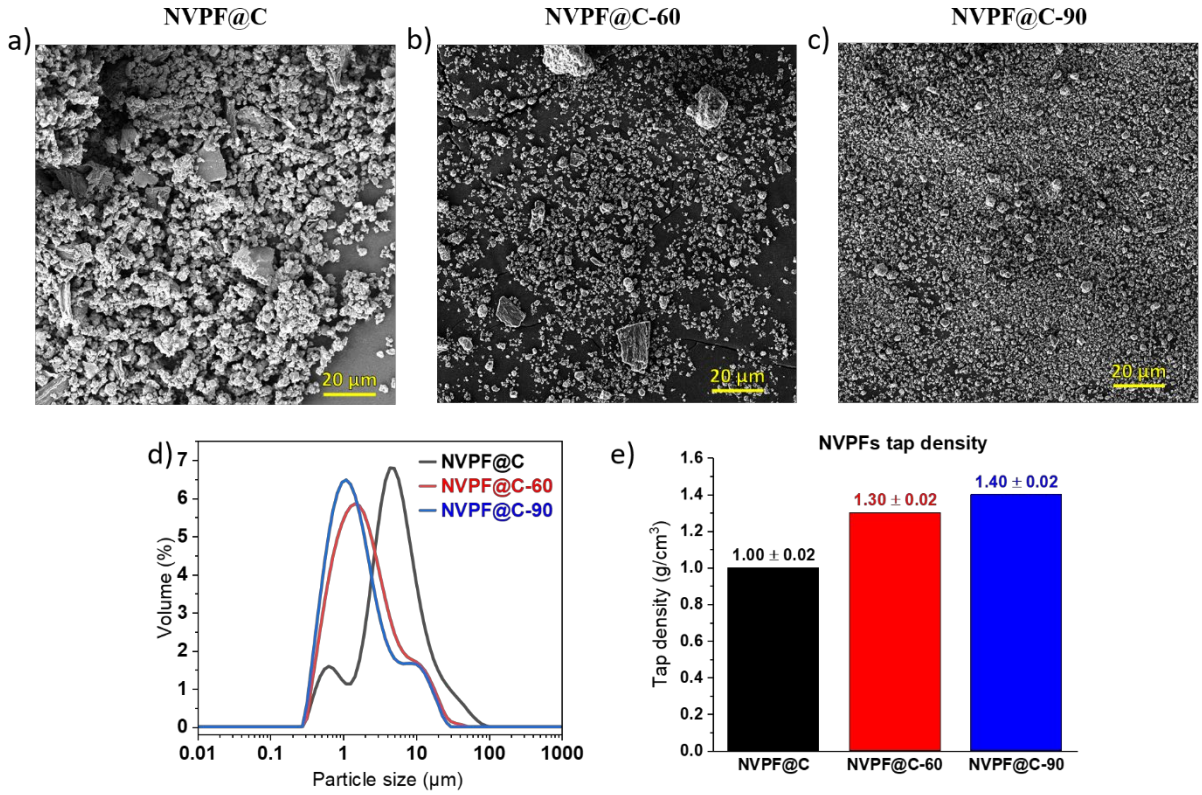

Figure 2. SEM images of a) NVPF@C, b) NVPF@C-60 and c) NVPF@C-90; Comparison of d) particle size distributions and e) tap densities for the three materials NVPF@C, NVPF@C-60 and NVPF@C-90.

Table 3. Comparison of the lattice parameters, average coherent domains size, specific surface area and tap density of NVPF@C, NVPF@C-60 and NVPF@C-90.

Sample	Lattice parameters (*Amam* space group)	Average coherent domains	Specific surface area	Tap Density
NVPF@C	a=9.0296(1) Å, b=9.0461(1) Å and c= 10.7551(1) Å	> 1000 Å	14.9 m^2/g	1 g/cm^3
NVPF@C-60	a=9.0311(1) Å, b=9.0492(1) Å and c= 10.7586(1) Å	820 Å	15.4 m^2/g	1.3 g/cm^3
NVPF@C-90	a=9.0300(1) Å, b=9.0488(2) Å and c= 10.7563(1) Å	690 Å	15.9 m^2/g	1.4 g/cm^3

Finally, this change in particle size distribution while keeping intact the crystal structure of the positive electrode material and the integrity of its carbon-coating leads to increase the tap density from 1 g/cm^3 to 1.3 g/cm^3 and 1.4 g/cm^3 for NVPF@C-60 and NVPF@C-90 respectively. This extremely favorable tap density is, to the best of our knowledge, significantly higher than all those reported in the literature among the family of (carbon-coated) $Na_3V_2(PO_4)_2F_{3-y}O_y$ positive electrode materials (see Table 1).

Based on these very promising results we decided to further investigate the effect of the ball-milling on the surface chemistry, which is of high importance for electrode materials, and has a direct impact on the electrochemical energy storage performance. For the further investigations we decided to focus on NVPF@C-90 due to its higher tap density and compare its characteristics to the sample before ball-milling.

One of the main risks during the mechanical grinding of a fluorinated active material coated with carbon is the reaction between both components leading to a possible surface degradation of the active material that can be detrimental for its performance and stability upon cycling. However, in this case, a comparison between the high-resolution F1s XPS spectra of NVPF@C and NVPF@C90 suggests an absence of reactivity. The main signal at 684.4 eV, characteristic of fluorine bonded to vanadium in $Na_3V_2(PO_4)_2F_3$, remains unchanged after the mechanical grinding, and the contribution attributed to C-F bonds at 686.5 eV remains negligible compared to the one corresponding to V-F bonds at 684.5 eV.[35] Likewise, the signal of V 2p that displays the presence of mixed V^{3+}/V^{4+} valence on the surface suggests that, although a low oxidation can be observed, the vanadium signal remains rather similar[34] These results suggest that despite particles and crystalline domains size decrease, the surface of $Na_3V_2(PO_4)_2F_3$ did significantly changed.

The unique significant change could be observed on the carbon spectra (Figure 3c for NVPF@C-90 *vs* Figure 3f for NVPF@C) and it highlights the fact that the carbon coating at the particles' surface became more disordered after the 90 minutes of mechanical grinding. A fitting of C 1s XPS spectra revealed a decrease in the amount of carbon sp^2 versus carbon sp^3 and a slight increase in the contribution peaking at 286.7 eV which is attributed to carbon linked to oxygen.[36] Besides, in the case of NVPF@C-90, the minimal contribution peaking at 290 eV which is typical for a carbon in close interaction with fluorine, remains very similar to the one

of pristine NVPF@C, confirming the negligible reactivity between the carbon and $Na_3V_2(PO_4)_2F_3$ phase.

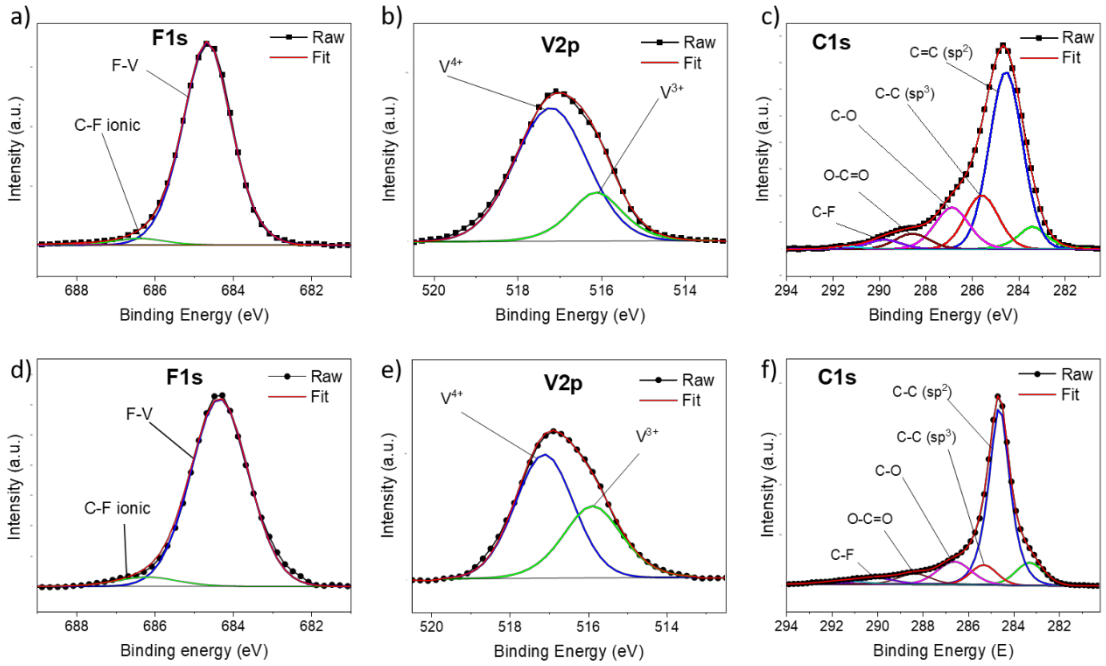

Figure 3. Fitted F 1s, V $2p_{3/2}$ and C 1s XPS spectra of NVPF@C-90 (a, b, c) and NVPF@C (d, e, f) materials.

After demonstrating that the consequent increase of tap density does not impact the bulk structure of the active material, nor its surface integrity (although a small surface oxidation was detected), in-depth electrochemical tests were conducted to evaluate the energy storage performance of NVPF@C-90 and compare them to those of NVPF@C. However, before comparing the specific capacities, rate capabilities and capacity retentions, it is important to highlight that electrode porosity decreased from 35% for NVPF@C to 27% for NVPF@C-90, although the same electrode preparation conditions were used for both active materials. This first observation aligns perfectly with the 40% higher tap density measured for NVPF@C-90 compared to NVPF@C.

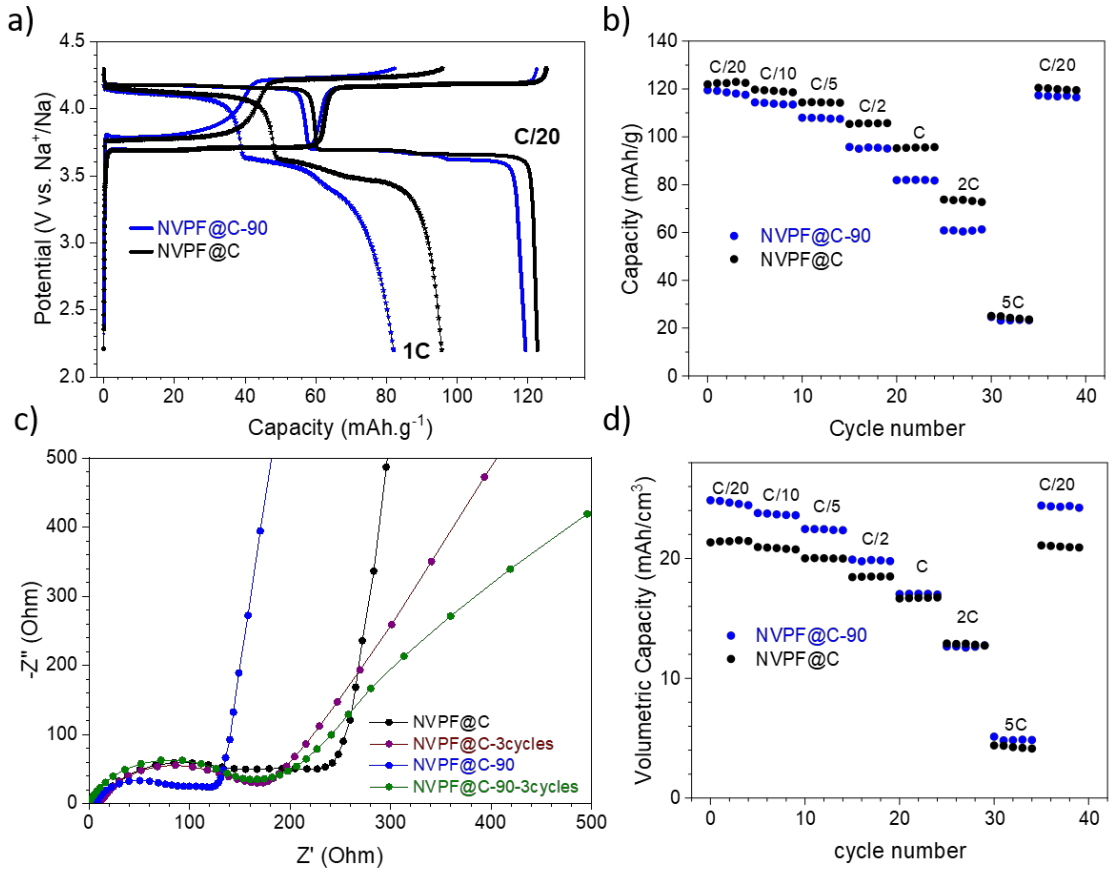

Figure 4. a) Comparison of galvanostatic charge-discharge curves at C/20 and 1C between NVPF@C and NVPF@C-90 containing electrodes; b) Rate capability tests performed from C/20 to 5C rates between 2.2 and 4.3V vs Na^+/Na; c) Nyquist plots of both samples for EIS conducted before cycling and after 3 formation cycles; d) Evolution of the volumetric capacity at various C-rates.

The galvanostatic charge/discharge curve of NVPF@C-90 measured at C/20 is very similar to that of NVPF@C (Figure 4a). In both case two reversible plateaus at 3.7 and 4.2 V vs Na^+/Na are observed, leading to a similar reversible specific capacity of 123 and 120 mAh/g for the pristine and the ball-milling electrode materials respectively. These results are expected considering the preservation of the crystal structure and the surface integrity of the active material, as just discussed. Nevertheless, charge/discharge cycles performed at faster rates have shown that the capacity retention decreases faster for NVPF@C-90 when the current density increases up to 2C, suggesting lower kinetics as the fully recovered initial capacity after the C-rate test refuted a material degradation upon cycling (Figures 4a-b). This lower kinetics might arise from excessively low porosity, which increases tortuosity within the electrode, hindering efficient ionic diffusion (resulting in higher ionic resistance). Additionally, the low overall porosity could generate closed pores, inaccessible to the electrolyte, rendering some portions of the NVPF@C-90 electrode material electrochemically inactive, thereby explaining the slightly lower capacity at low rates.[37] Indeed such a decrease of porosity has already been reported detrimental for the alkaline diffusion and rate performance.[38] This is supported by the electrochemical impedance spectroscopy measurements performed on both electrodes and reported on the Nyquist plots in Figure 4c. Before cycling the lower charge-transfer resistance observed for NVPF@C-90 compared to NVPF@C could be interpreted as a better percolation

network due to the lower porosity, but after three formation cycles at C/20, the charge transfer resistance characterized by the semi-circle at high frequencies become similar whereas the more horizontal slope at lower frequencies clearly revealed slower Na^+ diffusion for NVPF@C-90. On the other hand, it is interesting to point out that the increase in tap density led to higher volumetric capacities at rates up to 1C, and similar volumetric capacities at higher rates (Figure 4d). This perfectly illustrates the benefits of increasing tap density, especially for mobility applications where volumetric energy density is extremely important. Finally, prolonged cycling at C/5, illustrated in figure 5a, revealed for both materials an excellent capacity retention of 96% after 100 cycles with capacities of 103 mAh/g and 108 mAh/g for NVPF@C and NVPF@C-90 respectively. This excellent cycling stability suggests that the decrease of crystallinity and particle size do not impact the stability of the electrode material upon prolonged charge-discharge cycles. These first electrochemical results tend to demonstrate that, considering specific capacity, the lower high rate performance for the ball-milled based electrode are issued from lower Na-ion diffusion within the electrode due to a (too) low porosity within the electrode. On the other hand, the increase in tap density permits to enhance volumetric capacity of the electrode material.

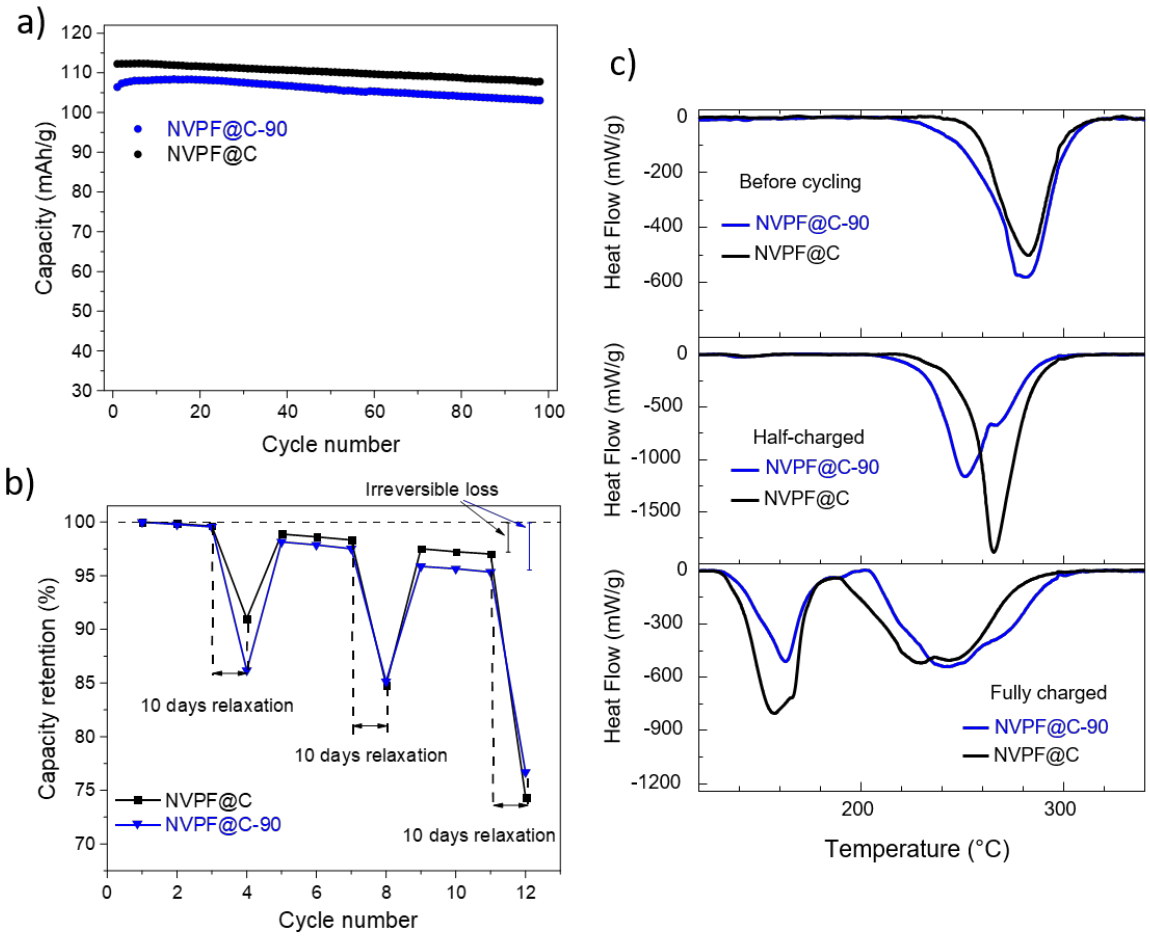

Figure 5. a) Evolution of specific capacity upon long-term cycling at C/5; b) Self-discharge tests for NVPF@C and NVPF@C-90 containing electrodes; c) Differential scanning calorimetry analyses to study the thermal stability of electrodes in contact with the electrolyte

at different states of charge. The half-charged material was recovered at 3.9V whereas the fully charged one was recovered at 4.3V vs Na^+/Na.

Additional experiments were also conducted to investigate the impact of this change in microstructure on the self-discharge of the electrode materials and their thermal stability at different states of charge. As represented in figure 5b, after 3 formation cycles performed at C/20, the electrodes are charged up to 4.3V and let relaxed for 10 days without applying any current nor potential. Then, the capacity retention is measured through a discharge down to 2.2V vs Na^+/Na and the full procedure is repeated 2 times. Initially, NVPF@C-90 shows higher self-discharge with capacity retention of 86% versus 91% for NVPF@C. However, similar capacity retentions (85%) are observed for the second self-discharge test and even slightly better one for NVPF@C-90 for the third self-discharge test. It can also be observed that for both electrode materials, the self-discharge at 25°C is important in a classical electrolyte and consequently increases with time.[39] Besides the irreversible capacity loss could be estimated after each relaxation period and is found to be more important for the ball-milled sample compared to the pristine one. Such more significant irreversible degradation could lead to the formation of a thicker electrode-electrolyte interface which finally might be beneficial and decrease the self-discharge as observed for the third relaxation step.

Table 4. Temperature values of the exothermic peak(s) and the total heat generated as calculated from data depicted in figure 5b.

	NVPF@C	NVPF@C-90
State of charge	Enthalpy and Peaks Maximum	Enthalpy and Peaks Maximum
Before cycling	90±7 J/g / 286±3°C	112±15 J/g / 282±3°C
Half-charged	260±30 J/g / 265±3°C	229±25 J/g / 251±3°C
Fully charged	322±10 J/g / 157±2°C and 230±2°C	311±11 J/g / 163±1°C and 241±2°C

Then, the impact of the ball-milling on the thermal stability of the carbon-coated $Na_3V_2(PO_4)_2F_3$ was investigated by DSC analyses of materials recovered at various states of charge and in contact with the electrolyte (Figure 5c). Before cycling, DSC curves for both NVPF@C and NVPF@C-90 are characterized by rather similar profiles with an exothermic signal peaking at ~ 280°C, in perfect agreement with the results reported by Pablos et al. for carbon-coated NVPF.[40] The enthalpy of the heat generated is slightly higher for the ball-milled material which may suggested a higher reactivity between the electrolyte salt and solvents, the polymer binder and the active material upon heating. These results can be explained by a more oxidized carbon coating as observed by XPS or to smaller particles and slightly larger specific surface areas. On the other hand, for both half-charged and fully charged materials, the experimental specific heats generated are lower for NVPF@C-90 compared to NVPF@C which highlights that although the particle's size decreases, the material reactivity upon heating does not increase (see Table 4). Dealing with degradation temperature, half-charged NVPF@C-90 starts to react at lower temperature compared to NVPF@C whereas the sample with the higher tapped density seems to be more thermally stable at fully charged state. Based on these results is it rather difficult to statute on which material is the most thermally stable but the lower heats generated for NVPF@C-90 compared to NVPF@C at charged states are benefic for practical purposes as it lowers the risk of thermal runaway.

Conclusion

The tap density of carbon-coated $Na_3V_2(PO_4)_2F_3$ was increased by 40% thanks to an innovative approach that consists in ball-milling material with micrometric shapeless morphology, leading to extremely favorable value of 1.4 g/cm^3. Comprehensive structural and microstructural investigations revealed that this mechanical process reduced both the particle and crystallite sizes without altering the structure or the composition of the active material. XPS experiments confirmed the absence of degradation or surface reactivity of $Na_3V_2(PO_4)_2F_3$ after the particle size reduction step. Besides, although XPS suggested a slightly more disordered and oxygen-rich carbon coating at the extreme surface, the overall Raman signature of the carbon remained unchanged after the mechanical grinding. Long-term cycling tests conducted for NVPF@C and NVPF@C-90 demonstrated an identical capacity retention of 96% after 100 cycles at C/5 showcasing their excellent stability upon cycling and the absence of detrimental effect due to particle size reduction. The slightly lower specific capacity retention at high rates measured for NVPF@C-90 was attributed to a too low electrode porosity which decreased from 35% to 27% and prevent efficient Na^+ diffusion due to less wettability of the electrode by the electrolyte, as confirmed by electrochemical impedance spectroscopy. On the other hand, the increase in tap density leads to an enhanced volumetric capacity, which is an important parameter for mobility applications. Nevertheless, electrode formulation still needs improvement to achieve a more suitable electrode porosity and, consequently, optimized rate performance. Self-discharge experiments revealed that compared to NVPF@C, it tends to be less pronounced over time for NVPF-90 whereas the irreversible capacity loss increases. Finally, no clear trend could be observed concerning the effect of microstructural changes on thermal stability of electrode materials. More globally, this study presents a rather counter-intuitive but efficient approach to increase tap density of carbon-coated $Na_3V_2(PO_4)_2F_3$ while preserving their structure and surface chemistry which could be applied to other polyanionic electrode materials.

Supporting Information

Full pattern matching refinements, Raman spectra, SEM images at different magnifications, TEM images.

Notes

The authors declare no competing financial interest.

Acknowledgement

The authors thank the French National Research Agency (STORE-EX Labex Project ANR-10-LABX-76-01 and the Project Nano-INSPIRE ANR-21-CE50-0006). The authors thank Cathy DENAGE, Eric LEBRAUD, Emmanuel PETIT and Jérôme KALISKY (ICMCB) for their technical support. The authors also thank Marie-Anne Dourges (Institut des Sciences Moléculaires) for the BET measurements.

References

(1) Hwang, J.-Y.; Myung, S.-T.; Sun, Y.-K. Sodium-Ion Batteries: Present and Future. *Chemical Society Reviews* **2017**, *46* (12), 3529–3614. https://doi.org/10.1039/C6CS00776G.

(2) Delmas, C. Sodium and Sodium-Ion Batteries: 50 Years of Research. *Advanced Energy Materials* **2018**, *8* (17), 1703137. https://doi.org/10.1002/aenm.201703137.
(3) Goikolea, E.; Palomares, V.; Wang, S.; Larramendi, I. R.; Guo, X.; Wang, G.; Rojo, T. Na-Ion Batteries—Approaching Old and New Challenges. *Advanced Energy Materials* **2020**, 2002055. https://doi.org/10.1002/aenm.202002055.
(4) Hasa, I.; Mariyappan, S.; Saurel, D.; Adelhelm, P.; Koposov, A. Y.; Masquelier, C.; Croguennec, L.; Casas-Cabanas, M. Challenges of Today for Na-Based Batteries of the Future: From Materials to Cell Metrics. *Journal of Power Sources* **2021**, *482* (September 2020), 228872–228872. https://doi.org/10.1016/j.jpowsour.2020.228872.
(5) Sada, K.; Darga, J.; Manthiram, A. Challenges and Prospects of Sodium-Ion and Potassium-Ion Batteries for Mass Production. *Advanced Energy Materials* **2023**, *13*, 2302321. https://doi.org/10.1002/aenm.202302321.
(6) Sayahpour, B.; Hirsh, H.; Parab, S.; Nguyen, L. H. B.; Zhang, M.; Meng, Y. S. Perspective: Design of Cathode Materials for Sustainable Sodium-Ion Batteries. *MRS Energy & Sustainability* **2022**, *9*, 197. https://doi.org/10.1557/s43581-022-00029-9.
(7) Hirsh, H. S.; Li, Y.; Tan, D. H. S.; Zhang, M.; Zhao, E.; Meng, Y. S. Sodium-Ion Batteries Paving the Way for Grid Energy Storage. *Advanced Energy Materials* **2020**, *10* (32), 2001274. https://doi.org/10.1002/aenm.202001274.
(8) Liang, X.; Hwang, J.-Y.; Sun, Y.-K. Practical Cathodes for Sodium-Ion Batteries: Who Will Take The Crown? *Advanced Energy Materials* **2023**, *13*, 2301975. https://doi.org/10.1002/aenm.202301975.
(9) Peng, J.; Zhang, W.; Liu, Q.; Wang, J.; Chou, S.; Liu, H.; Dou, S. Prussian Blue Analogues for Sodium-Ion Batteries: Past, Present, and Future. *Advanced Materials* **2022**, *34* (15), 2108384. https://doi.org/10.1002/adma.202108384.
(10) Li, Z.; Dadsetan, M.; Gao, J.; Zhang, S.; Cai, L.; Naseri, A.; Jimenez-Castaneda, M. E.; Filley, T.; Miller, J. T.; Thomson, M. J.; Pol, V. G. Revealing the Thermal Safety of Prussian Blue Cathode for Safer Nonaqueous Batteries. *Advanced Energy Materials* **2021**, *11* (42), 2101764. https://doi.org/10.1002/aenm.202101764.
(11) Masquelier, C.; Croguennec, L. Polyanionic (Phosphates, Silicates, Sulfates) Frameworks as Electrode Materials for Rechargeable Li (or Na) Batteries. *Chemical Reviews* **2013**, *113* (8), 6552–6591. https://doi.org/10.1021/cr3001862.
(12) Ni, Q.; Bai, Y.; Wu, F.; Wu, C. Polyanion-Type Electrode Materials for Sodium-Ion Batteries. *Advanced Science* **2017**, *4* (3), 1600275–1600275. https://doi.org/10.1002/advs.201600275.
(13) Nguyen, L. H. B.; Broux, T.; Camacho, P. S.; Denux, D.; Bourgeois, L.; Belin, S.; Iadecola, A.; Fauth, F.; Carlier, D.; Olchowka, J.; Masquelier, C.; Croguennec, L. Stability in Water and Electrochemical Properties of the Na3V2(PO4)2F3 – Na3(VO)2(PO4)2F Solid Solution. *Energy Storage Materials* **2019**, *20* (February), 324–334. https://doi.org/10.1016/j.ensm.2019.04.010.
(14) Mukherjee, A.; Sharabani, T.; Perelshtein, I.; Noked, M. Three-Sodium Ion Activity of a Hollow Spherical Na 3 V 2 (PO 4) 2 F 3 Cathode: Demonstrating High Capacity and Stability. *Batteries & Supercaps* **2020**, *3* (1), 52–55. https://doi.org/10.1002/batt.201900147.
(15) Desai, P.; Huang, J.; Foix, D.; Tarascon, J. Zero Volt Storage of Na-Ion Batteries : Performance Dependence on Cell Chemistry ! *Journal of Power Sources* **2022**, *551* (October), 232177–232177. https://doi.org/10.1016/j.jpowsour.2022.232177.
(16) Bianchini, M.; Fauth, F.; Brisset, N.; Weill, F.; Suard, E.; Masquelier, C.; Croguennec, L. Comprehensive Investigation of the Na 3 V 2 (PO 4) 2 F 3 –NaV 2 (PO 4) 2 F 3 System by Operando High Resolution Synchrotron X-Ray Diffraction. *Chemistry of Materials* **2015**, *27* (8), 3009–3020. https://doi.org/10.1021/acs.chemmater.5b00361.

(17) Broux, T.; Fauth, F.; Hall, N.; Chatillon, Y.; Bianchini, M.; Bamine, T.; Leriche, J.-B. J.; Suard, E.; Carlier, D.; Reynier, Y.; Simonin, L.; Masquelier, C.; Croguennec, L. High Rate Performance for Carbon-Coated Na 3 V 2 (PO 4) 2 F 3 in Na-Ion Batteries. *Small Methods* **2019**, *3* (4), 1800215. https://doi.org/10.1002/smtd.201800215.
(18) Chen, Z.-Y.; Zhang, L.-L.; Fu, X.-Y.; Yan, B.; Yang, X.-L. Synergistic Modification of Fe-Based Prussian Blue Cathode Material Based on Structural Regulation and Surface Engineering. *ACS Appl. Mater. Interfaces* **2022**, *14* (38), 43308–43318. https://doi.org/10.1021/acsami.2c11823.
(19) Rudola, A.; Rennie, A. J. R.; Heap, R.; Meysami, S. S.; Lowbridge, A.; Mazzali, F.; Sayers, R.; Wright, C. J.; Barker, J. Commercialisation of High Energy Density Sodium-Ion Batteries: Faradion's Journey and Outlook. *Journal of Materials Chemistry A* **2021**, *9* (13), 8279–8302. https://doi.org/10.1039/D1TA00376C.
(20) Zhang, Y.; Wang, Z.-B.; Nie, M.; Yu, F.-D.; Xia, Y.-F.; Liu, B.-S.; Xue, Y.; Zheng, L.-L.; Wu, J. A Simple Method for Industrialization to Enhance the Tap Density of LiNi0.5Co0.2Mn0.3O2 Cathode Material for High-Specific Volumetric Energy Lithium-Ion Batteries. *RSC Adv.* **2016**, *6* (70), 65941–65949. https://doi.org/10.1039/C6RA11052E.
(21) Zhang, Y.; Hou, P.; Zhou, E.; Shi, X.; Wang, X.; Song, D.; Guo, J.; Zhang, L. Pre-Heat Treatment of Carbonate Precursor Firstly in Nitrogen and Then Oxygen Atmospheres: A New Procedure to Improve Tap Density of High-Performance Cathode Material Li1.167(Ni0.139Co0.139Mn0.556)O2 for Lithium Ion Batteries. *Journal of Power Sources* **2015**, *292*, 58–65. https://doi.org/10.1016/j.jpowsour.2015.05.036.
(22) Thamodaran, P.; Murugan, V.; Sundaramurthy, D.; Sekar, K.; Maruthapillai, A.; Maruthapillai, T. Hierarchical Na 3 V 2 (PO 4) 2 F 3 Microsphere Cathodes for High-Temperature Li-Ion Battery Application. *ACS Omega* **2022**, *7* (30), 26523–26530. https://doi.org/10.1021/acsomega.2c02558.
(23) Olchowka, J.; Fang, R.; Bianchini Nuernberg, R.; Pablos, C.; Carlier, D.; Cassaignon, S.; Croguennec, L. Particle Nanosizing and Coating with an Ionic Liquid: Two Routes to Improve the Transport Properties of Na 3 V 2 (PO 4) 2 FO 2. *Nanoscale* **2022**, *14* (24), 8663–8676. https://doi.org/10.1039/D2NR01080A.
(24) Olchowka, J.; Nguyen, L. H. B.; Petit, E.; Camacho, P. S.; Masquelier, C.; Carlier, D.; Croguennec, L. Ionothermal Synthesis of Polyanionic Electrode Material Na 3 V 2 (PO 4) 2 FO 2 through a Topotactic Reaction. *Inorganic Chemistry* **2020**, *59* (23), 17282–17290. https://doi.org/10.1021/acs.inorgchem.0c02546.
(25) Li, L.; Xu, Y.; Sun, X.; He, S.; Li, L. High Capacity-Favorable Tap Density Cathode Material Based on Three-Dimensional Carbonous Framework Supported Na3V2(PO4)2F3 Nanoparticles. *Chemical Engineering Journal* **2018**, *331*, 712–719. https://doi.org/10.1016/j.cej.2017.09.012.
(26) Shen, C.; Long, H.; Wang, G.; Lu, W.; Shao, L.; Xie, K. Na3V2(PO4)2F3@C Dispersed within Carbon Nanotube Frameworks as High Tap Density Cathode for High-Performance Sodium-Ion Batteries. *Journal of Materials Chemistry A* **2018**, *6* (14), 6007–6014. https://doi.org/10.1039/C8TA00990B.
(27) Gao, J.; Tian, Y.; Ni, L.; Wang, B.; Zou, K.; Yang, Y.; Wang, Y.; Banks, C. E.; Zhang, D.; Zhou, K.; Liu, H.; Deng, W.; Zou, G.; Hou, H.; Ji, X. Robust Cross-Linked Na3V2(PO4)2F3 Full Sodium-Ion Batteries. *ENERGY & ENVIRONMENTAL MATERIALS* **2023**, *0*, e12485. https://doi.org/10.1002/eem2.12485.
(28) Cao, Y.; Li, X.-L.; Dong, X.; Liao, M.; Wang, N.; Cheng, J.; Xu, J.; Qi, Y.; Liu, Y.; Xia, Y. Pilot-Scale Synthesis Sodium Iron Fluorophosphate Cathode with High Tap Density for a Sodium Pouch Cell. *Small* **2022**, *18* (45), 2204830. https://doi.org/10.1002/smll.202204830.

(29) Rui, X.; Sun, W.; Wu, C.; Yu, Y.; Yan, Q. An Advanced Sodium-Ion Battery Composed of Carbon Coated Na3V2(PO4)3 in a Porous Graphene Network. *Advanced Materials* **2015**, *27* (42), 6670–6676. https://doi.org/10.1002/adma.201502864.
(30) Zhang, L.-L.; Liu, J.; Wei, C.; Sun, P.-P.; Gao, L.; Ding, X.-K.; Liang, G.; Yang, X.-L.; Huang, Y.-H. N/P-Dual-Doped Carbon-Coated Na 3 V 2 (PO 4) 2 O 2 F Microspheres as a High-Performance Cathode Material for Sodium-Ion Batteries. *ACS Applied Materials & Interfaces* **2020**, *12* (3), 3670–3680. https://doi.org/10.1021/acsami.9b20490.
(31) Jorio, A.; Souza Filho, A. G. Raman Studies of Carbon Nanostructures. *Annual Review of Materials Research* **2016**, *46* (1), 357–382. https://doi.org/10.1146/annurev-matsci-070115-032140.
(32) Bianchini, M.; Brisset, N.; Fauth, F.; Weill, F.; Elkaim, E.; Suard, E.; Masquelier, C.; Croguennec, L. Na3V2(PO4)2F3 Revisited: A High-Resolution Diffraction Study. *Chemistry of Materials* **2014**, *26* (14), 4238–4247. https://doi.org/10.1021/cm501644g.
(33) Lu, X.; Zhang, X.; Tan, C.; M. Heenan, T. M.; Lagnoni, M.; O'Regan, K.; Daemi, S.; Bertei, A.; G. Jones, H.; Hinds, G.; Park, J.; Kendrick, E.; L. Brett, D. J.; R. Shearing, P. Multi-Length Scale Microstructural Design of Lithium-Ion Battery Electrodes for Improved Discharge Rate Performance. *Energy & Environmental Science* **2021**, *14* (11), 5929–5946. https://doi.org/10.1039/D1EE01388B.
(34) Fang, R.; Olchowka, J.; Pablos, C.; Camacho, P. S.; Carlier, D.; Croguennec, L.; Cassaignon, S. Effect of the Particles Morphology on the Electrochemical Performance of Na 3 V 2 (PO 4) 2 F 3-y O y. *Batteries & Supercaps* **2022**, *5* (1), 1–10. https://doi.org/10.1002/batt.202100179.
(35) Gu, Z.-Y.; Guo, J.-Z.; Sun, Z.-H.; Zhao, X.-X.; Li, W.-H.; Yang, X.-L.; Liang, H.-J.; Zhao, C.-D.; Wu, X.-L. Carbon-Coating-Increased Working Voltage and Energy Density towards an Advanced Na3V2(PO4)2F3@C Cathode in Sodium-Ion Batteries. *Science Bulletin* **2020**, *10* (43), 36851–36859. https://doi.org/10.1016/j.scib.2020.01.018.
(36) Shen, W.; Li, H.; Wang, C.; Li, Z.; Xu, Q.; Liu, H.; Wang, Y. Improved Electrochemical Performance of the Na3V2(PO4)3 Cathode by B-Doping of the Carbon Coating Layer for Sodium-Ion Batteries. *J. Mater. Chem. A* **2015**, *3* (29), 15190–15201. https://doi.org/10.1039/C5TA03519H.
(37) Elango, R.; Nadeina, A.; Cadiou, F.; De Andrade, V.; Demortière, A.; Morcrette, M.; Seznec, V. Impact of Electrode Porosity Architecture on Electrochemical Performances of 1 Mm-Thick LiFePO4 Binder-Free Li-Ion Electrodes Fabricated by Spark Plasma Sintering. *Journal of Power Sources* **2021**, *488*, 229402. https://doi.org/10.1016/j.jpowsour.2020.229402.
(38) Heubner, C.; Nickol, A.; Seeba, J.; Reuber, S.; Junker, N.; Wolter, M.; Schneider, M.; Michaelis, A. Understanding Thickness and Porosity Effects on the Electrochemical Performance of LiNi0.6Co0.2Mn0.2O2-Based Cathodes for High Energy Li-Ion Batteries. *Journal of Power Sources* **2019**, *419*, 119–126. https://doi.org/10.1016/j.jpowsour.2019.02.060.
(39) Yan, G.; Reeves, K.; Foix, D.; Li, Z.; Cometto, C.; Mariyappan, S.; Salanne, M.; Tarascon, J.-M. A New Electrolyte Formulation for Securing High Temperature Cycling and Storage Performances of Na-Ion Batteries. *Advanced Energy Materials* **2019**, *9* (41), 1901431. https://doi.org/10.1002/aenm.201901431.
(40) Pablos, C.; Olchowka, J.; Petit, E.; Minart, G.; Duttine, M.; Weill, F.; Masquelier, C.; Carlier, D.; Croguennec, L. Thermal Stability of Na3–XV2(PO4)2F3–YOy: Influence of F– for O2– Substitution and Degradation Mechanisms. *Chem. Mater.* **2023**, *35* (10), 4078–4088. https://doi.org/10.1021/acs.chemmater.3c00539.